LASER INTERFEROMETER GRAVITATIONAL WAVE OBSERVATORY
- LIGO -
CALIFORNIA INSTITUTE OF TECHNOLOGY
MASSACHUSETTS INSTITUTE OF TECHNOLOGY

Technical Note	**LIGO-T1900281–v1**	2020/10/11

High Fidelity Probe of Optical Scatter from Point Defects

Author: Kruthi K
Mentors: Gautam Venugopalan, Koji Arai, Rana Adhikari

California Institute of Technology
LIGO Project, MS 18-34
Pasadena, CA 91125
Phone (626) 395-2129
Fax (626) 304-9834
E-mail: info@ligo.caltech.edu

Massachusetts Institute of Technology
LIGO Project, Room NW22-295
Cambridge, MA 02139
Phone (617) 253-4824
Fax (617) 253-7014
E-mail: info@ligo.mit.edu

LIGO Hanford Observatory
Route 10, Mile Marker 2
Richland, WA 99352
Phone (509) 372-8106
Fax (509) 372-8137
E-mail: info@ligo.caltech.edu

LIGO Livingston Observatory
19100 LIGO Lane
Livingston, LA 70754
Phone (225) 686-3100
Fax (225) 686-7189
E-mail: info@ligo.caltech.edu

http://www.ligo.caltech.edu/

Acknowledgements

I would like to thank my mentors Gautam Venugopalan and Arai Koji for patiently answering all my questions and helping me out with everything. This work would have been incomplete without their invaluable insights and support. I'm grateful to Prof. Rana Adhikari for helping me recognize the goals of the project and driving me to work towards them. I would also like to thank Charles Osthelder (Chub) for constantly helping with all the hardware. Special thanks to Prof. Alan Weinstien for going out of his way to make all the LIGO SURFs feel at home. This list would be incomplete without a mention of all members of the LIGO Scientific Collaboration(LSC), IndIGO and the LIGO SURF Program who have all played a key role in enriching this experience. I would like to thank the SURF community, the Student Faculty Programs Office and California Institute of Technology for facilitating this program.

Contents

1 Introduction **1**

2 Project **1**

2.1 Problem 1

2.2 Approach and Objectives 2

3 The Setup **3**

4 Telescope design **4**

4.1 Ray transfer matrix analysis 5

4.2 Optimization of parameters for the MC2 camera 7

5 Acquisition of Image of the MC2 Mirror **8**

6 Scatter Loss Measurements **8**

6.1 Radiometric calibration of CCD camera 8

6.2 Scatter loss map 10

7 Understanding the image **12**

7.1 Intensity Profile 12

7.2 HDR images 13

7.3 HDR Algorithm 15

8 Detection of Point Defects **16**

9 Future Work **17**

References **18**

1 Introduction

Gravitational waves (GWs) are ripples in the fabric of spacetime generated by accelerated masses, that propagate as waves at the speed of light. Their existence was predicted by Albert Einstein's General Theory of Relativity in 1916 and the possibility of using interferometers to detect the gravitational waves was first considered in the early 1960s. After several decades of research and technological upgradations, aLIGO became capable of detecting the extremely small amplitude of gravitational waves. This led to its first detection of gravitational waves, from a black hole coalescence, on 14th September 2015. Gravitational waves provide us a lot of information about their sources such as black holes, neutron stars and so on, and act as a novel tool to probe our universe further.

LIGO consists of a ground based network of laser interferometers designed to detect gravitational waves from distant astrophysical sources in the frequency range - 10 Hz to 10 kHz [1]. The infinitesimal gravitational wave strain is obtained by measuring the variations in the intensity of the recombined light at the detection port, which is a function of the differential arm length (DARM) of the interferometer. It exploits several advance modifications to the usual Michelson interferometer, such as four stage suspension of test masses for seismic isolation [2], highly stable laser - which is about a 100 million times more stable than an ordinary laser - to increase the resistance to intensity noise, test masses made of fused silica to minimize IR absorption, extremely smooth optical coatings to reduce scatter loss, large test masses - with a diameter of 34cm and weight around 40kg - to keep the radiation pressure noise to a level comparable to the suspension thermal noise [3], and use of Fabry-Perot cavity inside each arm to increase their interaction time with gravitational waves through multiple reflections, to increase its potency. Currently, its strain sensitivity is more than 10^{-23} $1/\sqrt{Hz}$ around 100Hz, which is millions of times smaller than a proton! But to further increase the strain sensitivity, understanding the noise sources - fundamental, technical and environmental - is critical .

2 Project

2.1 Problem

LIGO's mirrors/test masses have been specifically designed and constructed with multi-layered interference coatings via ion-beam deposition to minimize optical absorption, mirror thermal noise and light scattering [6]. The fused silica material used for the input test masses is an ultra-low absorption grade, with absorption at 1064 nm of less than 0.2 ppm/cm and is extremely smooth [2].

However, the laser light striking the test masses is still subject to scatter in spite of these precautions. An ideal mirror would appear black when viewed off axis from a source of illumination incident normally on the mirror; the photographs of an Advanced LIGO End Test Mass, illuminated by the 100 kW beam, taken at an angle of 9.8° to the main beam (figure 1), rather show a large number of light scattering points [6].

Scattering of light reduces the power circulating in the Fabry-perot cavities leading to a lower signal to noise ratio. It also leads to the decoherence of the scattered laser light. The

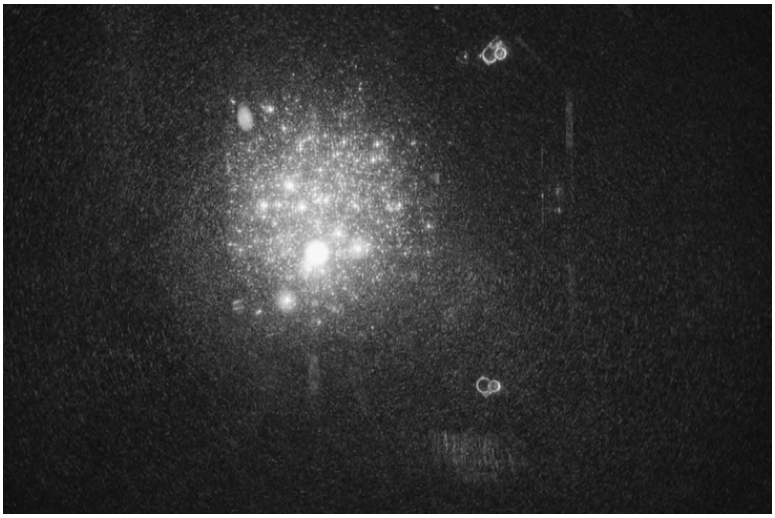

Figure 1: Photograph of an aLIGO End Test Mass; exposure time of 1.3 seconds [6].

backscattered light, from the moving chamber walls, baffles, mirrors, or photodiodes, couples into the main beam as shown in figure 2 and modulates the phase and amplitude of main beam, introducing a random phase noise [1].

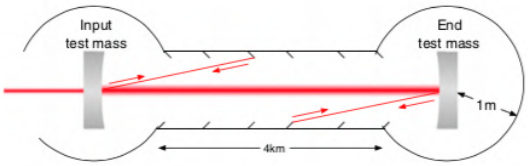

Figure 2: Scattering inside the arm cavity [1]

In order to develop techniques to further reduce the scattering and design optical cavities with lower losses, we, first off, need repeatable and reliable methods to characterize the scatter loss, understand the nature of scattered light and study scattering due to surface imperfections, point scatters, coating, etc.

2.2 Approach and Objectives

This project aims to use an existing camera system, currently being used to monitor the beamspot on the mirrors/test masses, to study the scattering at large angles. The camera system consists of analog cameras installed inside cylindrical enclosures that are mounted on top of a view-port along the beam tube, as shown in figure 3. With these analog cameras, we don't have control over exposure time and the image of the beamspot is highly saturated. By using digital cameras (referred as GigE cameras here), we can extract lot more information about the scattered light and the point defects on the surface of the mirrors/test masses.

The plan is to, first, install a GigE camera for one of the Mode Cleaner mirrors (MC2),

do some studies with it and later on, implement a similar camera setup for all the optical cavities in the lab.

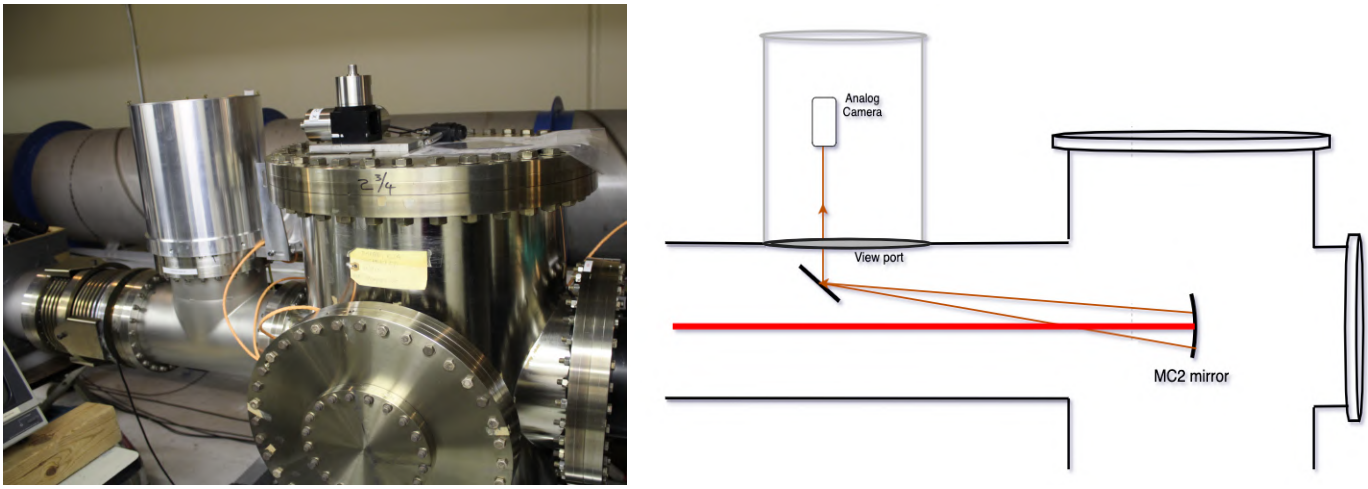

Figure 3: Existing MC2 camera system

3 The Setup

MC2 mirror was chosen to implement the trial model of the setup, as its view-port along the beam tube is easily accessible compared to other cavity chambers in the lab. While in the trail phase, instead of completely replacing the analog camera with GigE camera, it is useful to have both the cameras operating simultaneously. So, different configurations for co-mounting the two cameras inside the cylindrical enclosure were explored. After taking all the hardware constraints, and pros and cons of other configurations into consideration, we decided to implement the configuration shown in figure 4.

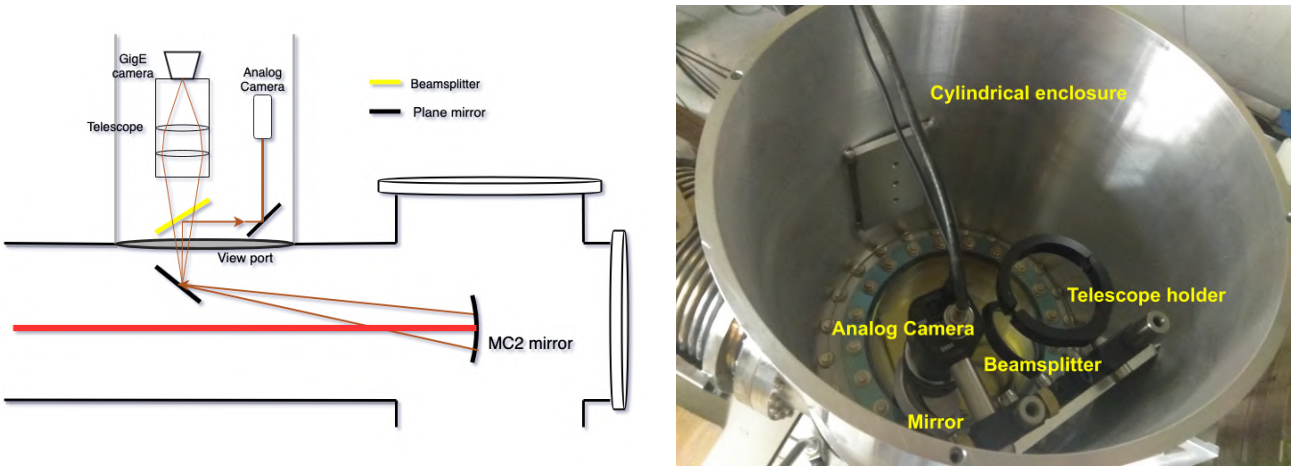

Figure 4: MC2 camera setup

In the above setup, we have a plane mirror inclined at 45° to the main beam tube, inside the vaccuum chamber. The light scattered from the MC2 mirror that falls onto this mirror is further passed through a beamsplitter. The beamsplitter being used has a 5° wedge and eliminates ghosting. A two lens telescope system is used to focus the beam spot onto the GigE camera sensor while ensuring optimum utilization of the CCD pixel array. By using another plane mirror as shown, we are able to simultaneously monitor the beam spot with the analog camera.

4 Telescope design

Placing a telescopic lens system between the camera and vacuum viewport to get focused images (as shown in figure 7) gives us access to a variety of focal plane distances and helps us control the field of view captured, in contrast to the use of single camera lens. A Python program was used to select an appropriate combination of focal lengths amongst the available options such that the combination can focus the entire optic (3" diameter) as well as the beam spot ($\sim$ 2mm diameter) by varying the distance between the lenses. Following are the considerations made while choosing the lenses:

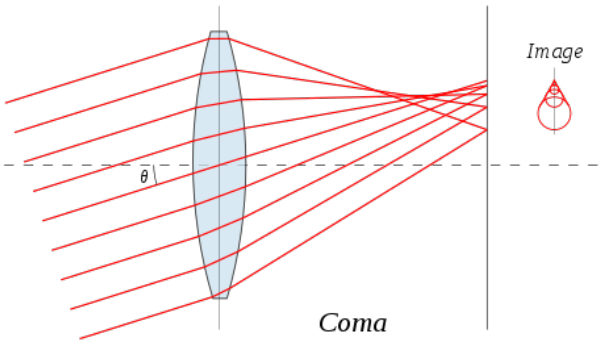

Figure 5: Coma Aberration

- As we are required to get real images of the optic to focus on CCD sensor, plano-convex or biconvex lenses are to be used.
- As the laser light used is of 1064nm, the lenses need to be V-AR coated at 1064nm to reduce the scattering and enable maximum transmission at this wavelength.
- Lenses with larger diameter collect more light, hence 2" lenses are preferred over 1" lenses.
- As the conjugate ratio is greater than 5, plano-convex lenses offer a better approximation to the bestform lenses that reduce the effects of spherical aberrations.
- Lenses with f-numbers greater than 5 are preferred as spherical aberrations are less pronounced in them.
- The lenses are to be chosen such that the image formed at the focal plane, i.e., the camera sensor, utilizes maximum number of pixels possible.
- Rays traversing in off axis regions produce varying transverse magnification leading to coma (figure 5). To reduce this effect we can judiciously place an aperture, or a stop, in the optical system so that most of the marginal rays are eliminated [11].

Along with these, constraints on dimensions of various hardware components (like cylindrical enclosures, slotted lens tubes, etc), possible range of object distances, available options for hardware components, etc., are to be considered.

4.1 Ray transfer matrix analysis

The process of imaging through several optical elements can be described by a 2×2 matrix, M, called the ray transfer matrix or the system matrix.

$$\begin{bmatrix} y' \\ \theta' \end{bmatrix} = M \begin{bmatrix} y \\ \theta \end{bmatrix} \qquad \text{where } M = \begin{bmatrix} m_{11} & m_{12} \\ m_{21} & m_{22} \end{bmatrix} \tag{1}$$

Here y, y', θ and θ' represent object height, image height, angle made by the ray with the principal axis at object plane and at image plane respectively (see figure 6).

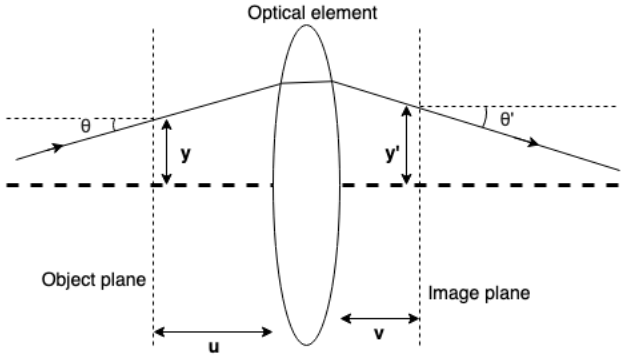

Figure 6: Schematic for understanding system matrix

For any optical element with ray transfer matrix $\begin{bmatrix} A & B \\ C & D \end{bmatrix}$ and an object placed at a distance u, the system matrix M is given by following equation:

$$M = \begin{bmatrix} 1 & v \\ 0 & 1 \end{bmatrix} \begin{bmatrix} A & B \\ C & D \end{bmatrix} \begin{bmatrix} 1 & u \\ 0 & 1 \end{bmatrix}$$

$$\implies M = \begin{bmatrix} A + Cv & Au + Cuv + B + Dv \\ C & Cu + D \end{bmatrix} \tag{2}$$

The imaging condition imposed is such that light rays incident, irrespective of the incident angles, in the paraxial approximation, converge to the same image plane. This sets the imaging criteria to be $m_{12} = 0$. Therefore, we have

$$Au+Cuv+B+Dv=0 \implies \text{v} = \frac{-Au - B}{Cu + D} \tag{3}$$

If the input and output planes are located within the same medium, or within two different media which happen to have identical indices of refraction, then the determinant of M is equal to 1. Thus, in our case, $m_{11}m_{22} = 1$; this implies

$$A + Cv = \frac{1}{Cu + D} \tag{4}$$

Additionally, from equation 1 the relation between the output and input height becomes

$$\text{image height(y}') = (A + Cv) \times \text{object height(y)}$$

Thus we have,

$$\text{magnification} = A + Cv = \frac{1}{Cu + D} \tag{5}$$

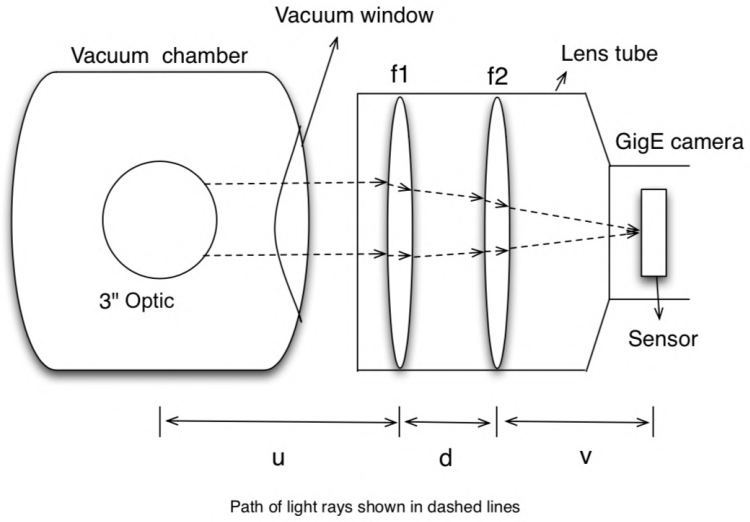

Figure 7: Schematic of the telescopic lens system [5]

The optical element here is a combination of two lenses of focal lengths f_1 and f_2, separated by distance d. Thus, the ray transfer matrix is given by

$$\begin{bmatrix} A & B \\ C & D \end{bmatrix} = \begin{bmatrix} 1 & 0 \\ -1/f_1 & 1 \end{bmatrix} \begin{bmatrix} 1 & d \\ 0 & 1 \end{bmatrix} \begin{bmatrix} 1 & 0 \\ -1/f_2 & 1 \end{bmatrix}$$

$$\implies \begin{bmatrix} A & B \\ C & D \end{bmatrix} = \begin{bmatrix} (1 - d/f_2) & d \\ (-1/f_1 - 1/f_2 + d/f_1 f_2) & (1 - d/f_1) \end{bmatrix} \tag{6}$$

The above equation gives the values of A, B, C and D for given combination of two lenses. Note that the element C is representative of the effective focal length of the two lens system, i.e., C = $\frac{-1}{f_{eff}}$.

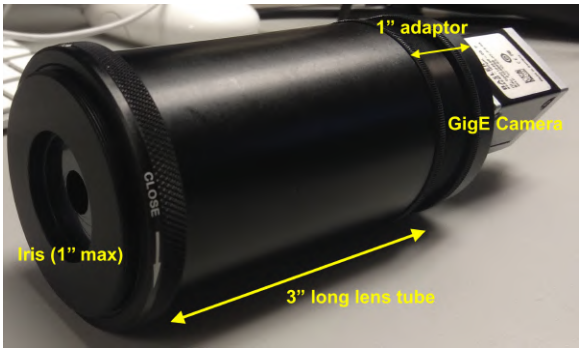

Figure 8: Picture of telescope designed for MC2 camera setup

4.2 Optimization of parameters for the MC2 camera

The available aluminium cylindrical enclosures were of lengths 52cm and 24cm. The 52cm long enclosure is heavier and mounting it on the beam tube might not be safe. So, we decided to go with the 24cm long enclosure, but this greatly limits the length of lens tube that can be used for the telescope. Amongst the available options for the lens tube, we found a 3″ long slotted lens tube to be the most appropriate one as it could be easily fitted inside the cylindrical enclosure. The GigE camera is directly attached to the lens tube using a thread adaptor. This implies the distance between the lenses (d) plus the distance to the image plane (v) is more or less fixed.

The optical path length between the MC2 mirror and the telescope is around 70cm, and this can be increased by a maximum of 5cm (refer figure 4). The available options for focal length of the two lenses were 50, 100, 125, 150, 200, 250, 300 & 500 mm.

The CCD sensor has dimensions 2.8mm × 3.7mm. The required magnification (m), for an image circle circumscribing the sensor, with the object size ranging from 3 inches for the surface of the entire optic to 2mm for focusing on the beam spot, lies between 0.068 to 0.18.

The following table summarizes the above discussion:

Parameters	**Possible range of values**
f_1, f_2	50, 75, 100, 125, 150, 200, 250, 300, 500 mm
v + d	7cm - 10 cm
u	70cm - 75 cm
m	0.068 - 0.18

Using the equations 3, 5, 6 and the above constraints, we were able to choose suitable focal lengths for the two lenses with the help of a Python code. The figure 8 shows the telescope designed for MC2 camera. It consists of two bi-convex lenses of 150mm focal length, separated by approximately 1cm. Here, the 1″ long lens tube adaptor helps us fine-tune the distance to image plane and the iris allows us to control the aperture size.

5 Acquisition of Image of the MC2 Mirror

The camera used for the purpose of this project is Basler ace acA640-120gm. It is equipped with a Gigabit Ethernet(GigE) interface and gets its power via PoE (Power over Ethernet) cable. A Power over Ethernet(PoE) connection is one wherein a single connection over ethernet cables provides both power and a connection for data transmission. This reduces the number of connections and complexity of the network. On the other hand, the GigE interface provides a framework for high speed transmission of data over ethernet network thereby increasing the speed of response, improving the control over camera settings and enabling a faster and real time data acquisition and computation.

A GigE camera equipped with the telescope described in section 4.2, was installed inside the cylindrical enclosure mounted on top of the MC2 view-port along the beam tube, as shown in figure 4. Basler's camera software Pylon and few other python scripts were used to interact with the camera. Pylon allows us to capture images at exposure levels varying from 4μs to 1s. The figure 9 shows an image of beam spot on MC2 mirror captured with an exposure time of 300μs.

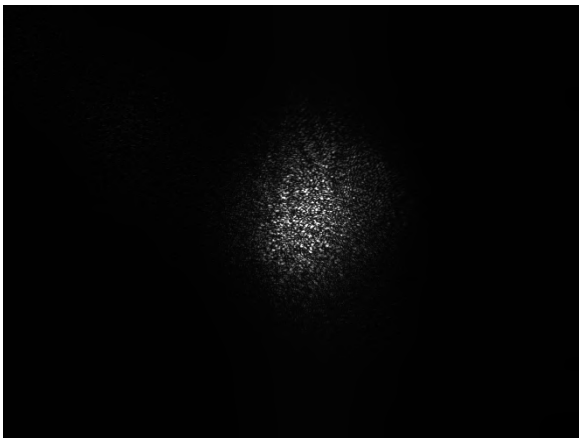

Figure 9: Image of beamspot on the MC2 mirror with an exposure of 300μs

6 Scatter Loss Measurements

6.1 Radiometric calibration of CCD camera

While employing a CCD camera to make quantitative power measurements the recorded pixel values must be decoded as radiance. The opto-electronic conversion function which maps physical power to a pixel value might vary for each pixel due to manufacturing variations in the CCD elements. Hence, radiometric calibration is used to characterize the variations in the conversion function (i.e., the calibration factor) the across the sensor [5].

The scattered power (P_s) is then calculated from the images of the calibrated CCD according to the following equation,

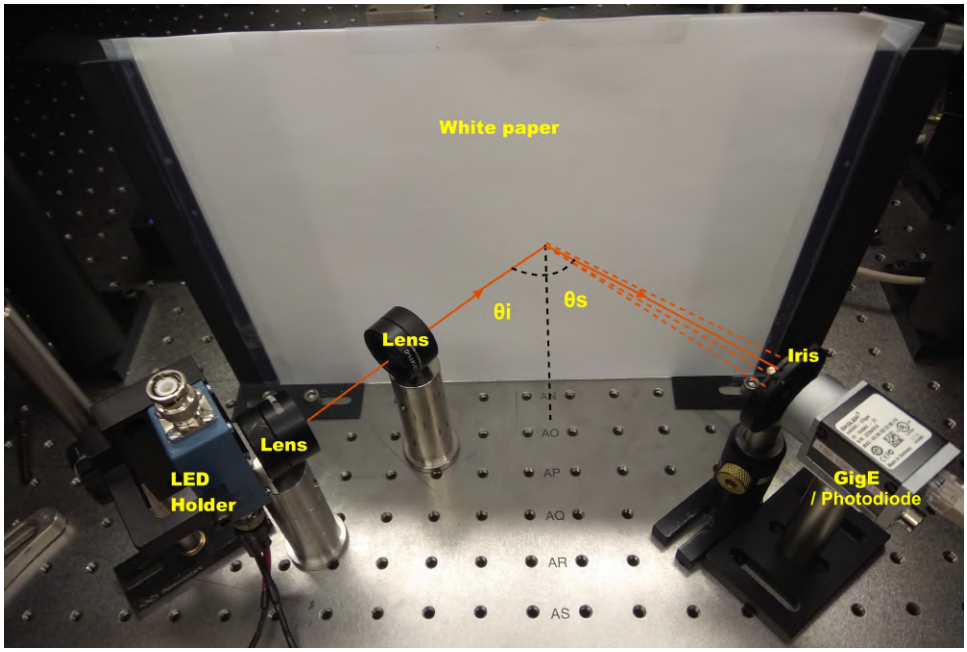

Figure 10: Setup for Radiometric Calibration

$$P_s = CalibrationFactor(CF) \times \frac{\sum_{ROI} PixelValue}{ExposureTime} \tag{7}$$

where ROI is the region of interest selected around the beam spot in the captured images. Here the pixel counts are summed over the ROI and normalized by the camera exposure time.

A CCD sensor records the number incoming light photons in terms of pixel counts which is representative of the number of electrons emitted from the sensor. The image as a two dimensional array contains these pixel counts. Within the saturation limit, the sum of pixel count of an image varies linearly with the number of photons incident, which in turn varies as power $\times$ exposure time. Thus, for a fixed incident power (P_s) the sum of pixel count varies linearly with exposure time. If the pixels saturate, the additional light that hits the sensor is not registered in the image and hence, our power estimation will yield an inaccurate value.

Figure 10 shows the setup used for radiometric calibration of a CCD camera. With a laser source, the lowest possible incident power is still high enough to easily saturate the images for low exposure times. Hence, we have used a 1050nm LED instead of a laser source. The white paper which is a Lambertian scatterer acts a uniform secondary light source. The calibration factor of a given CCD camera can be obtained by making a comparative measurement between the camera and a photodetector. This involves taking snapshots of a uniform light source (which is the scattered light from white paper in our case) for different exposure times for a fixed incident power, plotting pixel sum against exposure time as shown in figure 11, and using the slope of this plot to calculate the CF as given by equation 8.

$$\text{Calibration factor (CF)} = \frac{\text{Power incident on the CCD sensor}}{\text{slope of pixel sum vs exposure time plot}} \tag{8}$$

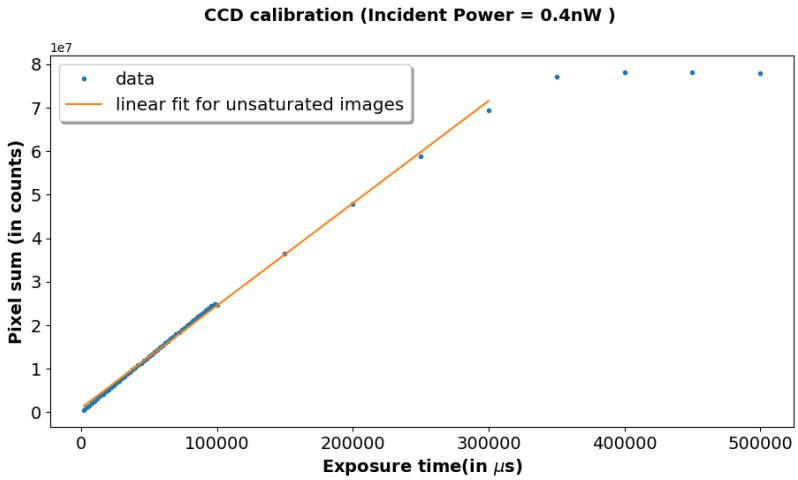

Figure 11: Graph for obtaining Calibration Factor (CF)

The incident power on the CCD sensor is measured by placing a photodetector in its place. The relationship between photodetector reading and power incident on the CCD sensor is given by:

$$\frac{\text{Photodector reading}}{\Omega_{photodetector}} = \frac{\text{Power incident on the CCD sensor}}{\Omega_{CCD\ sensor}} \tag{9}$$

where $\Omega_{photodetector}$ and $\Omega_{CCD\ sensor}$ are solid angles subtended by the photodetector and the CCD sensor respectively, at the centre of LED light spot on the white paper. This arises from the fact that our secondary light source is uniform, i.e., luminous intensity is constant across any cross section perpendicular to the source.

By following the steps described above, we obtained a calibration factor of 2.14×10^{-15} W-sec/counts.

6.2 Scatter loss map

The position of the beam spot on MC2 mirror was shifted by varying the pitch and yaw offsets of the Wavefront Sensor (WFS). The plot shown in figure 12 gives us the relation between offset values of WFS and actual position of the beam spot on the mirror. Here, the centre of the mirror is taken as the origin for the coordinates (also refer MC2 diagram in figure 13).

The scatter loss for different positions of the beam spot was obtained by taking snapshots with the GigE camera and converting the pixel sum of each image to corresponding power units, using formula 8. Note that the measured power of scattered light corresponds to the light scattered at a particular angle, not the total light scattered, as our setup collects scattered light only at a fixed angle as seen in figure 4.

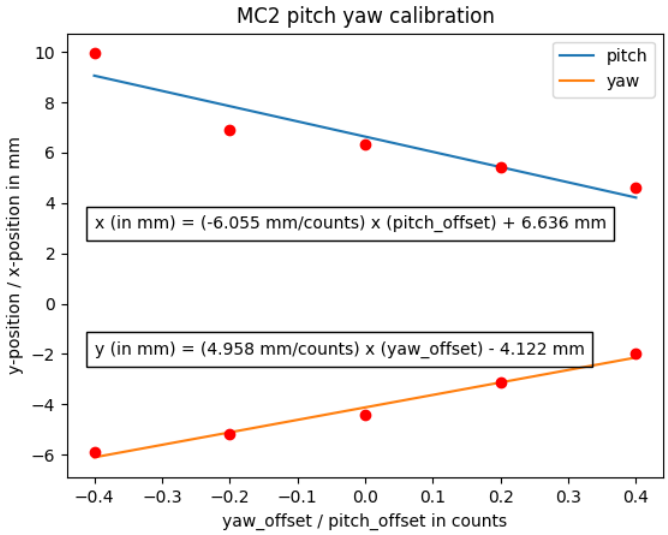

Figure 12: MC2 position vs offset

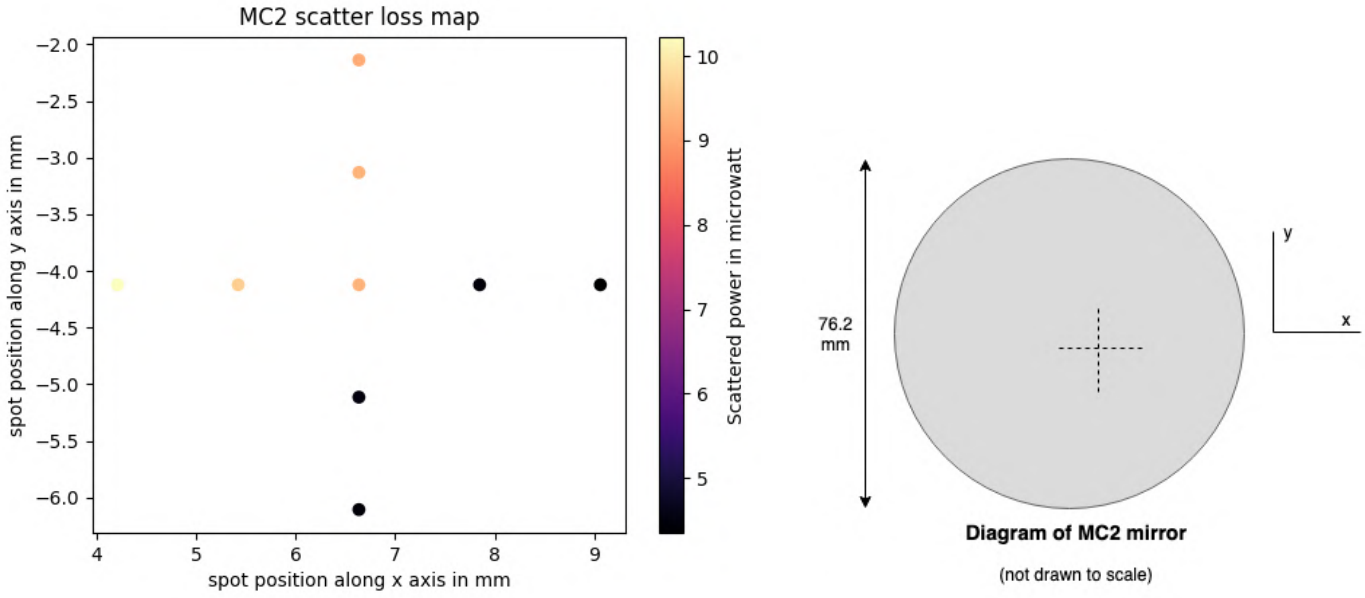

Figure 13: MC2 scatter loss map

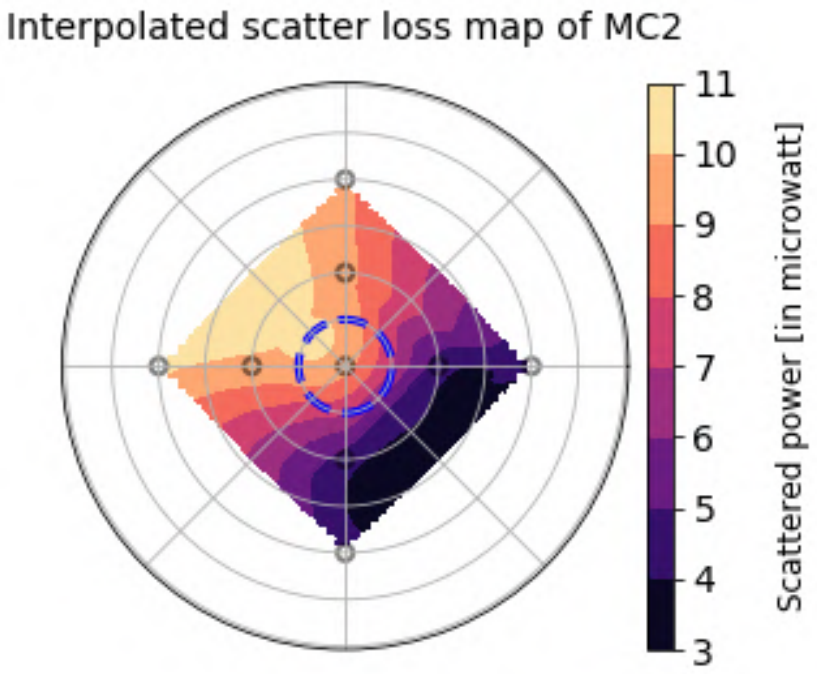

Figure 14: Interpolated scatter loss map of MC2 mirror. (Radial lines are at graduations of 0.1 offset, blue dashed circle indicates approximate beam size, solid circles are points at which beam was centered on MC2 for loss measurement)

Figure 13 shows a surface plot of scatter loss vs x and y positions of the beam spot. Hight amount of scattering indicates large number of point defects in that region. With the help of such scatter loss map we can easily identify the regions on the mirror with maximum number of point defects. This way, we can centre the beam spot on a region with less or no points defects, thereby reducing the loss due to scattering of light.

7 Understanding the image

7.1 Intensity Profile

The normal modes supported by an optical cavity are Hermite-Gaussian modes. In absence of any scattering effects, we would expect a Gaussian intensity profile. For an unsaturated image the pixel value is directly proportional to the intensity. Thus the intensity value corresponding to each pixel can be calculated using the following equation,

$$\text{Intensity}_{(\text{at each pixel})} = \frac{\text{CF} \times \text{Pixel value(in counts)}}{\text{Pixel size} \times \text{Exposure time}} \tag{10}$$

On plotting the intensity vs pixel number along a particular axis of the image of the beam spot on the MC2 mirror, as shown in figure 15, we see that the intensity profile deviates quite a bit from the expected Gaussian profile. This deviation is mainly caused due to scattering

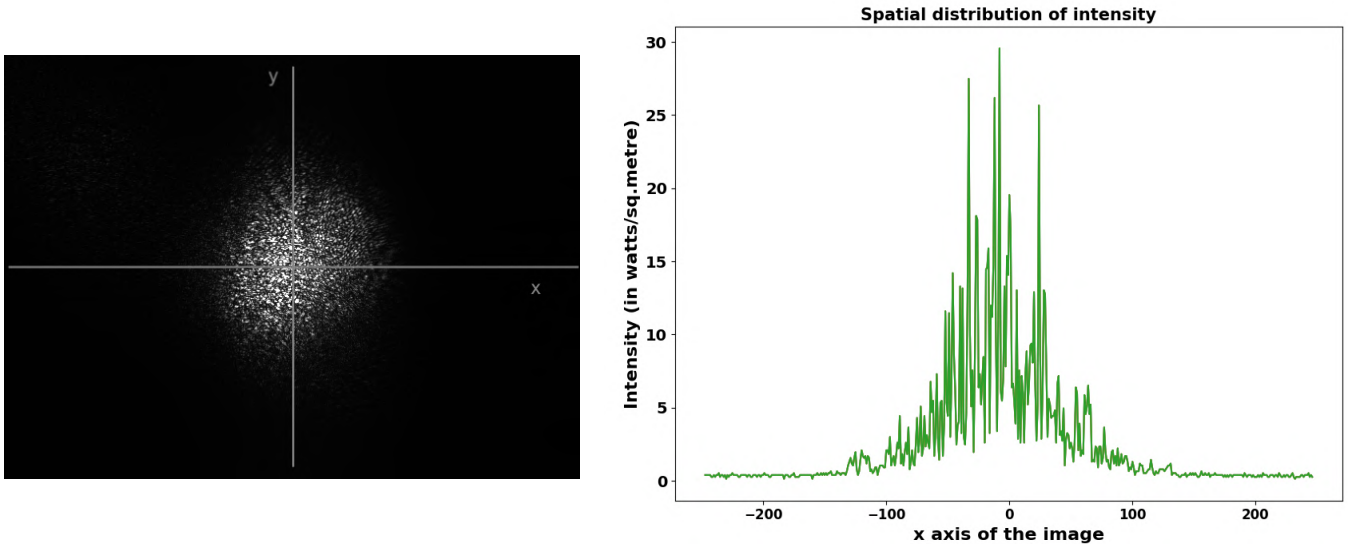

Figure 15: Deviation from Gaussian Intensity Profile

from point defects. A more comprehensive analysis of the above image can reveal a lot more information about the point defects.

7.2 HDR images

Dynamic range describes the ratio between the maximum and the minimum measurable light intensities. An ordinary scene illuminated by both direct and obstructed sunlight can have a dynamic range of 10^5. The human eye can actually perceive a greater dynamic range than ordinarily possible with a camera. This is because while a human eye is capable of continuously readjusting to capture sensitive information, the camera just captures the frame without accounting for any of the dynamic brightness gradients or contrasts among other features.

Even if one's digital camera could capture a vast dynamic range, the precision at which light measurements are translated into digital values may limit usable dynamic range. This precision is described in terms of bit-depth. For example, A 10-bit image can only encode a contrast ratio of 1024:1 even if the actual scene has a much higher dynamic range. Currently, the only standard solution for encoding a nearly infinite dynamic range is to use high dynamic range (HDR) imaging [12].

A color coded plot is used to display the HDR image (figure 16). The bit depth of the images captured by the camera is a parameter which can be controlled while operating the camera. It can either be set to 8 or 12. The HDR image produced by the algorithm uses several images captured at a given bit depth at different exposures, however, captures a finer subtlety in intensity. This is made possible as the pixels can assume a larger range of values. In effect, this implies that the algorithm produces an image which has a higher bit depth.

The plot in figure 17 depicts the image histogram for an ordinary 12-bit image and a HDR image of MC2. Clearly, the pixel values extend over a larger range in the HDR image. As we can see, for the HDR image the contrast ratio is approximately 35000:1, which is equivalent

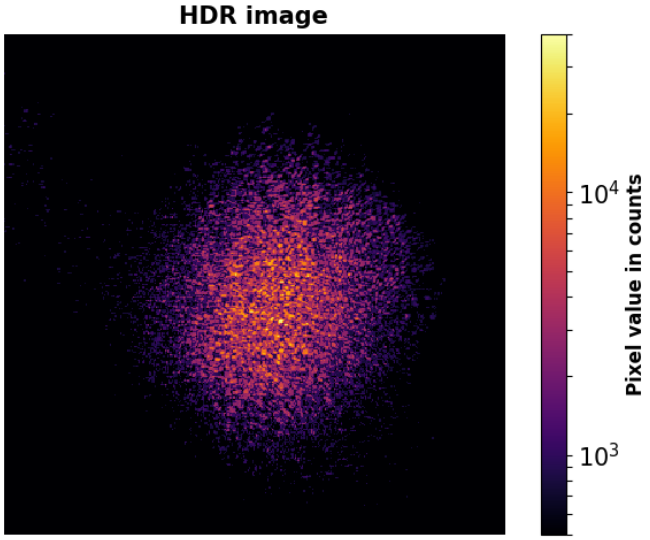

Figure 16: Color coded HDR image of MC2 beamspot

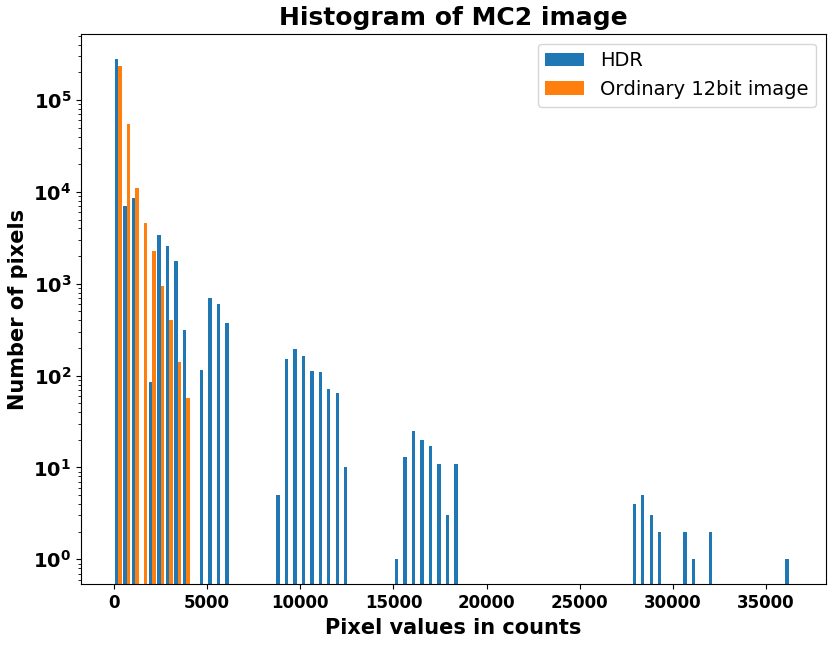

Figure 17: Histogram comparing a HDR image with an ordinary image

to a bit-depth of 15. As the HDR image can resolve the contrast and image details much better than an ordinary image, it helps us study the size, spatial distribution and brightness of point defects in a better way.

7.3 HDR Algorithm

A Python program that superimposes images captured at various exposure times onto one another after scaling them with an appropriate factor, identified as the ratio of exposure times, was used to create the HDR images. It replaces the saturated pixel on one image with an unsaturated pixel from the other image being superposed. This eliminates saturation in the resulting image to a large extent.

The HDR algorithm we have used differs from the commonly employed tone-mapping algorithms which control the brightness and contrast of the image, and are more concerned with adapting the final image content to view on a display device by uniformly scaling the pixel values, thereby limiting the image in terms of dynamic range [5].

Camera response function (CRF) maps scene irradiance to image intensities. For unsaturated images CRF is linear, and it becomes non-linear as the images get saturated [8]. CRF can be estimated from the images if we know the exposure times for each image [9]. Until the pixel values reach a certain threshold value, CRF can be approximated to a linear function, beyond that, the approximation fails (see figure 18). The threshold value is specific to a particular camera and can be determined easily from the CRF. In our case, it was around 250 for 8 bit images and 4000 for 12 bit images.

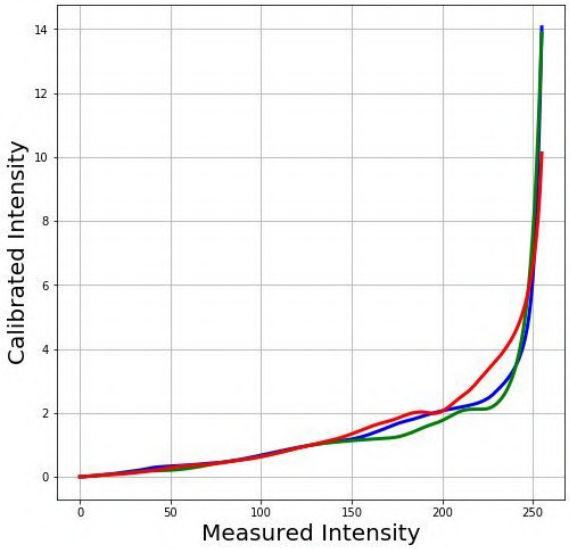

Figure 18: An example of camera response function [7]

In the algorithm given below, brightness value of a pixel is defined as the ratio of the pixel value to the exposure time of the image. The input array of images should contain images of different exposures - underexposed, properly exposed and overexposed. In our case, a properly exposed image is taken to be the one whose highest pixel value is 244 or 4095,

for an 8-bit and 12-bit image, respectively. The underexposed images are darker than the properly exposed image and capture regions that are very bright. The overexposed images are brighter than the properly exposed image and capture regions that are very dark. Scale factor is a numerical factor that converts pixel values to integers [7].

Algorithm 1: The HDR algorithm

Input: An array of images *img* in ascending order of their exposure time $t[i]$'s
Output: Corresponding HDR image

```
// initialize bvHDR to brightness value of lowest-exposure image
bvHDR ← img[0]/t[0]
for i in range 1 to max index of the array do
    bvAB ← img[i]/t[i]
    // use brightness value from bvHDR where img[i] is saturated
    foreach pixel where img[i] > threshold do
        Replace that pixel in bvAB with a corresponding pixel from bvHDR
    a bvHDR ← bvAB
imHDR ← bvHDR × scaleFactor(bvHDR)
Function scaleFactor(image):
    Arrange pixel values in an order
    sf ← mode of difference between consecutive values
    return sf
```

8 Detection of Point Defects

The images of a beam spot are similar in appearance to star clusters. Therefore, they can be analyzed with stellar photometry packages like DAOPHOT or Photutils [6]. These packages provide functions designed specifically to detect point-like sources in an image. The detection algorithm searches images for local density maxima that have a peak amplitude greater than a specified *threshold* and a size and shape similar to a defined 2D Gaussian kernel. The Gaussian kernel is defined by the $fwhm$, *ratio*, *theta*, and *sigma_radius*. These quantities are amongst the few other input parameters that are to be optimized.

The background and the background noise levels were estimated using sigma-clipped statistics. In this method, pixels that are above or below a specified *sigma_level* from the median are discarded briefly, and the image median and standard deviation are calculated. The procedure is typically repeated over a number of iterations or until convergence is reached. If the background level and the noise are relatively constant across the image, the values that the image median and the standard deviation converge to are taken as the image background and 1-sigma background noise, respectively.

As the background or the background noise might vary across the image, it is better to employ a 2D background that is estimated by applying the above techniques to subregions (boxes) of the image.The *box_size* should be chosen such that the boxes are larger than the

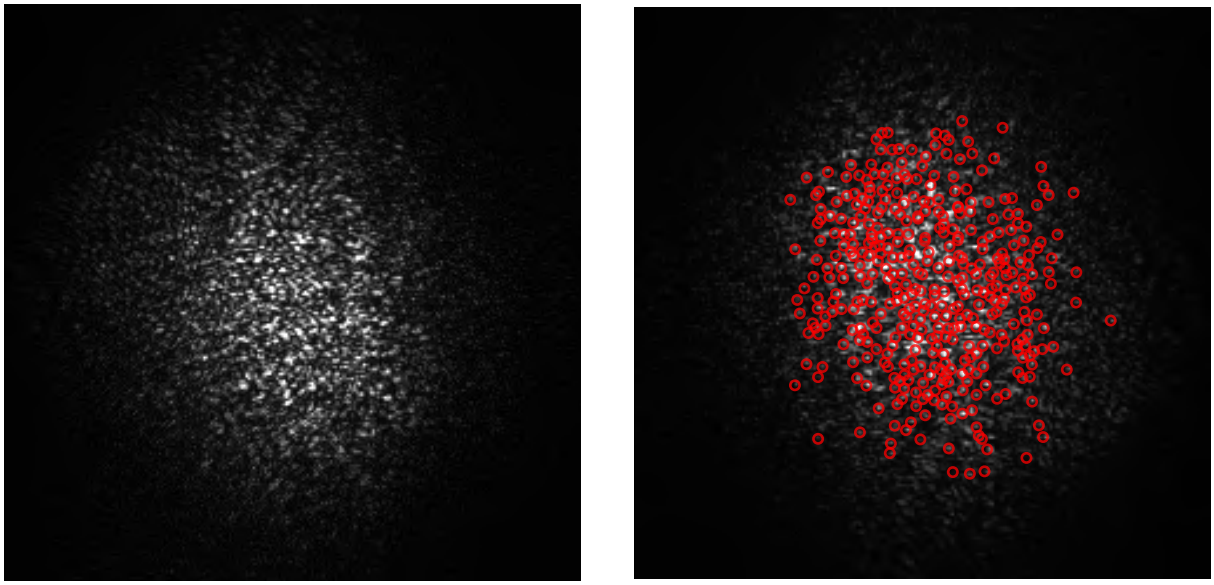

Figure 19: Photograph of MC2 beam spot (left); Exposure time of 0.3 milliseconds. Same image with the location of detected point scatterers marked (right).

typical size of scatterers in the image, but are small enough to capture the variations. After the background level has been determined in each of the boxes, the generated 2D background can be median filtered, with a window of size of $filter\_size$, to suppress the errors in local estimations [14].

Figure 19 shows the point scatterers detected in the MC2 optic. The main challenge with using the above approach to detect point scatterers is optimization of various input parameters such us the $threshold$, box_size, $sigma\_level$, $filter\_size$, etc. Further, the light scattered by each of the point-scatterers can be estimated using Aperture photometry or PSF photometry tools provided by Photutils.

9 Future Work

- Installation of GigE cameras for all cavities.
- Design for real time measurements of scattered light at small angles.
- Estimation of the size, spatial distribution and fraction of light scattered by the point scatterers.
- Investigate if it is possible to get some info about the coherence of scattered light and the effect of different coatings on scattering from these images.

References

[1] D.V. Martynov et al., *Sensitivity of the Advanced LIGO detectors at the beginning of gravitational wave astronomy* Phys. Rev. D 93, 112004 (2016)

[2] www.ligo.caltech.edu/page/ligo-technology

[3] www.ligo.caltech.edu/page/optics

[4] Nuttall LK, *Characterizing transient noise in the LIGO detector* Phil. Trans. R. Soc. A 376: 20170286. (2018)

[5] Jigyasa Nigam, Mentors: Gautam Venugopalan, Johannes Eichholz, *Characterization of Test Mass Scattering*. LIGO-SURF Report (2017).

[6] L.Glover et al., *Optical scattering measurements and implications on thermal noise in Gravitational Wave detectors test-mass coatings* Physics Letters A. 382. (2018)

[7] Mallick, Satya. "High Dynamic Range (HDR) Imaging Using OpenCV (C++/Python)" Learn OpenCV, 2 Oct. 2017, www.learnopencv.com/high-dynamic-range-hdr-imaging-using-opencv-cpp-python/

[8] Fu. L and Qi. Y *Camera Response Function Estimation and Application with a Single Image* Lecture Notes in Electrical Engineering, 149–156 (2011)

[9] Debevec, P. E. and Malik, J. (1997) *Recovering high dynamic range radiance maps from photographs* DOI:10.1145/258734.258884

[10] Yoshinori Akao, Norimichi Tsumura, Toshiya Nakaguchi and Yoichi Miyake, *Characterization of white paper sheets by BRDF model parameters estimated in the specular reflection plane* Journal of Imaging Science and Technology 54, no. 6 (2010): 60503-1.

[11] Fundamental Optics www.cvimellesgriot.com

[12] "Dynamic Range in Digital Photography." Cambridge in Colour, www.cambridgeincolour.com/tutorials/dynamic-range.htm

[13] Fabian Magana-Sandoval, Rana Adhikari, Valera Frolov, Jan Harms, Jacqueline Lee, Shannon Sankar, Peter R. Saulson and Joshua R Smith, *Large-angle scattered light measurements for quantum-noise filter cavity design studies*. Technical Note LIGO-T1400252-LSC. (2014)

[14] Bradley, et al. User Documentation, Photutils. Astropy/Photutils: v0.7.2, Dec. 2019 photutils.readthedocs.io/en/stable/index.html.